LA-UR-17-30052
Approved for public release; distribution is unlimited.

Title:	Laser Additive Manufacturing of F/M Steels for Radiation Tolerant Nuclear Components
Author(s):	Lienert, Thomas J. Maloy, Stuart Andrew
Intended for:	Report
Issued:	2017-11-02

Final Report for Phase 1 (a) and (b) Results: "Laser Additive Manufacturing of F/M Steels for Radiation Tolerant Nuclear Components"

20170591ER

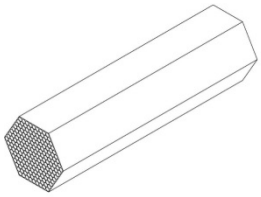

T.J. Lienert - PI

Sigma Division

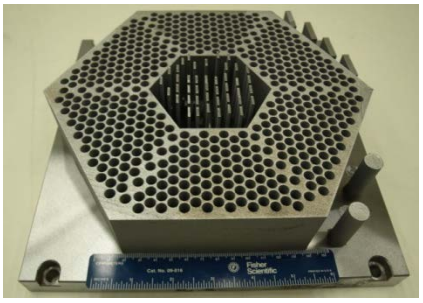

Contributors:

MST-8
Stuart Maloy (Sci IV) – PI
Eda Aydogan (Post Doc) - Investigator
Ben Eftink (Post Doc) - Investigator
Ricardo Lebensohn (Sci IV) – Investigator
Laurent Capolungo (Sci III) – Investigator
Daniel Vega
Rod McCabe
Carl Cady

MST- 16
Terry Holesinger
Matthew Janish
Todd Steckley

MPA-CINT
Nathan Mara
Jordan Weaver

Sigma Division
Robin Pacheco (R&D Eng I) - Investigator
Mike Brand (R&D Eng I) - Investigator
Cameron Knapp
Geoff Swank

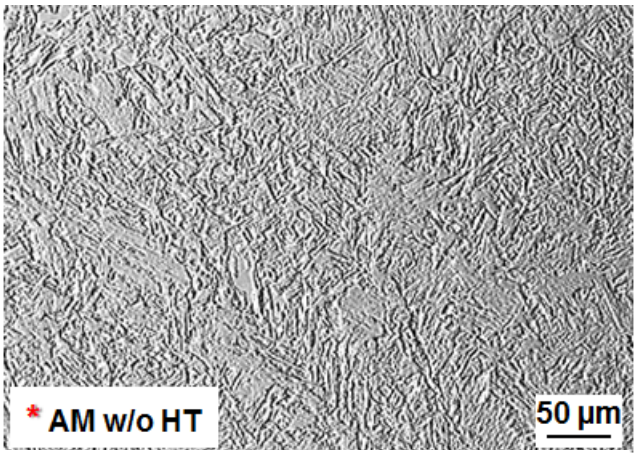

Martensitic microstructure desired for Gr91 F/M steel components in reactor service.

Introduction

According to the Nuclear Energy R&D Roadmap Report submitted to Congress in 2010, one the key challenges facing the nuclear energy industry involves development of new reactor designs with reduced capital costs. Two related R&D objectives outlined in the report include: 1) Making improvements in the affordability of new reactors; and 2) Development of structural materials to withstand irradiation for longer periods. Laser additive manufacturing (LAM) is particularly well suited for more rapid and economical fabrication of reactor components relative to current fabrication methods. The proposed work involving LAM directly addresses the two R&D objectives outlined above relevant to the pertinent mission problems.

The classical Materials Science approach involving development of Process/Structure/Property/Performance (P/S/P/P) relations was employed in this project. Processing included LAM and heat-treating. Thermal cycling during LAM is discussed here, and phase diagrams and continuous cooling transformation (CCT) diagrams are used to rationalize microstructural evolution. Structures were characterized including grain size & morphology, volume fraction, morphology, composition and location of carbides in as-deposited and heat-treated conditions. In the simplest sense, the goal was to control microstructures through process manipulation with a view toward optimizing properties and performance in service.

Materials

The original plan for this study involved LAM of a heat of Grade 92 (Gr 92) steel powder that was custom made. However, a heat of a similar steel powder, Gr 91, was found to be immediately available at lower costs. The Gr 91 steel was purchased to streamline project costs and schedule.

Substitution of Gr 91 for Gr 92 in this project is not a real concern, since the two alloys are nearly identical in composition and performance. Both alloys are referred to as modified 9% Cr alloys, and both are described as creep resistant ferritic steels (CRFS). It is important to note that results developed with Gr91 are directly pertinent to Gr 92, as well as other CRFS's.

Modified 9Cr–1Mo–V–Nb steel (aka Gr 91) was developed in the late 1970's by Combustion Engineering and Oak Ridge National Laboratory (ORNL). Gr 91 steel is a 2nd generation creep-resistant F/M steel with 9% Cr, 1% Mo and small additions of V and Nb to form fine carbo-nitrides. It is currently employed broadly in fossil and nuclear power plants in both plate and piping forms for components operating at temperatures up to ~650°C. Gr 91 is the current "workhorse" alloy in these applications and was approved for use under the ASME Boiler and Pressure Vessel (B&PV) Code in 1983.

Gr 92 steel is a 3rd generation creep-resistant F/M steel with 9% Cr, 2% W, and small additions of V and Nb to form fine carbo-nitrides. The V and Nb contents are lowered relative to Grade 91 to reduce activation during irradiation. Gr 92 steel has markedly better creep properties, at least for shorter times, relative to Gr 91, but has

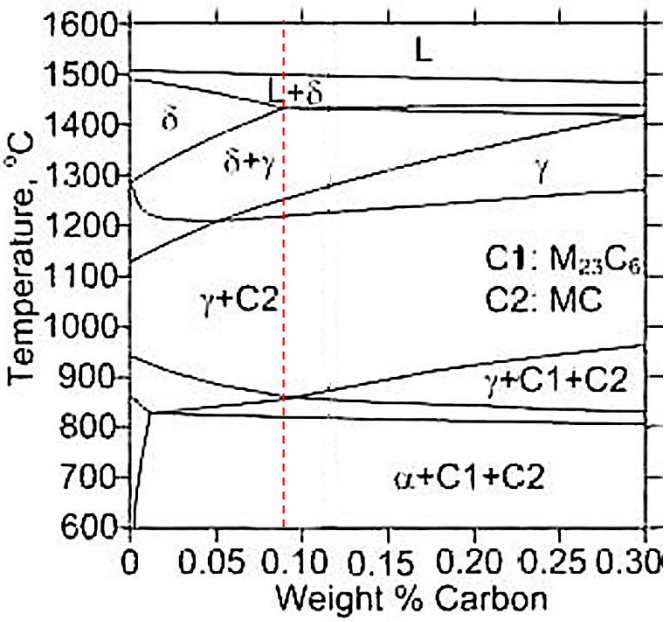

Figure 1 – Calculated pseudo-binary phase diagram for Gr 91 steel. The red line corresponds to 0.09% C.

not been code qualified. It may someday supplant Gr 91 as the preferred alloy. However, it is important to note that recent long-term creep issues have been identified recently with Gr 92.

A pseudo-binary section of the phase diagram calculated for Gr 91 is shown in Figure 1. The phase diagram indicates the equilibrium phases as a function of temperature and composition, in this case as a function of C content. The red dashed line corresponds to 0.09% C, the composition for the heat of powder used in this study. The diagram also designates the sequence of equilibrium phases present during cooling from the liquid phase (L > δ > γ>α, including two types of carbides).

Since phase diagrams cannot be used to predict non-equilibrium transformation, it is useful to refer to a continuous cooling transformation (CCT) diagram such as that for Gr 91 shown in Figure 2. As seen in the CCT diagram, a non-equilibrium phase, referred to as Martensite, can form from cooling of the austenite phase (≥1050°C) at all cooling rates greater than ~0.05°C/s.

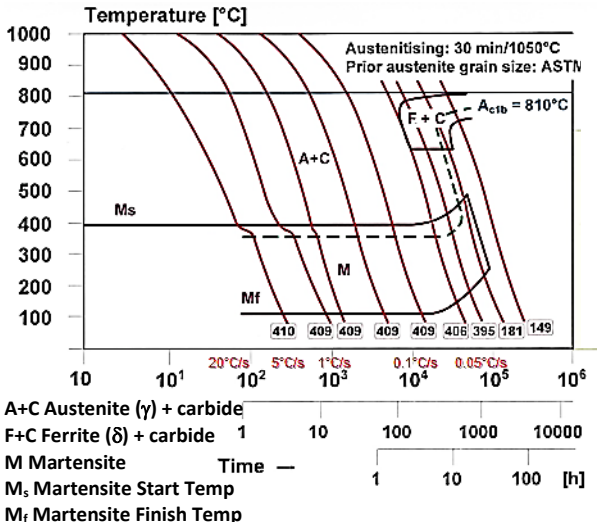

Figure 2 – Continuous cooling transformation (CCT) diagram such as that for Gr 91.

Objectives

Overall, the proposed efforts were aimed at providing a LAM-based solution for precision fabrication of affordable nuclear reactor components and addressing fabrication of components with a-priori design for radiation tolerance. High-level R&D goals for the study included: 1) determining the feasibility of LAM for affordable fabrication of reactor components from a creep resistant steel, specifically Grade 91 (Gr 91), with improved radiation tolerance; and 2) fabricating a scaled prototype reactor component.

Experimental Procedures

Materials

A heat of Gr91 steel powder was purchased from Carpenter Powder Products (Bridgeville, PA). The powder was produced using atomization in nitrogen. The composition of the powder, as well as the compositions for Gr91 and Gr92 from pertinent specifications are shown in Table 1. Note that the compositions for Gr91 and Gr92 are nearly identical, as discussed above (see underlined values). Gr92 contains slightly less Mo, with specified additions of W and B. Also, notice that the heat of powder complies with the specification except for a slightly higher Ni content.

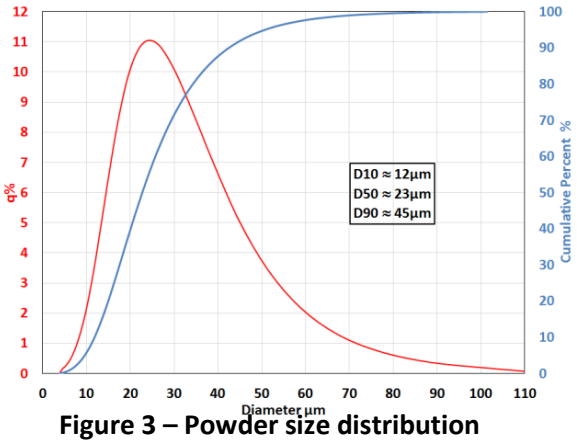

Figure 3 – Powder size distribution data for Gr 91 powder.

The powder size distribution was characterized using laser scattering analysis with a Horiba analyzer. Information on the powder size distribution is provided in Figure 3. The q% represents the volume percent determined for each diameter range. The powder diameters ranged from about 5 µm to over 100 µm, with 90% of the powder less than ~45 µm. The values for D10, D50 and D90 by volume are shown in the plot.

	Grade 91 Composition Specification (wt.%)*	Grade 91 Composition Powder Alloy (wt.%)	Grade 92 Composition Specification (wt.%)*
C	0.08-0.12	0.09	0.07-0.13
Mn	0.30-0.60	0.47	0.30-0.60
P	0.020	0.003	0.020
S	0.010	0.007	0.010
Si	0.20-0.50	0.41	0.50
Cr	8.00-9.50	9.01	8.50-9.50
Mo	*0.85-1.05*	0.93	*0.30-0.60*
Ni	0.040	*0.06*	0.040
V	0.18-0.25	0.18	0.15-0.25
Nb	0.06-0.10	0.07	0.04-0.09
B	-	<0.001	*10-60 ppm*
N	0.03-0.07	0.03	0.03-0.07
Al	0.040	0.02	0.040
Ti	-	<0.01	-
W	-	-	*1.50-2.00*
Zr	-	<0.01	-
Fe	Rem	Rem	Rem

Table 1– Composition of the Gr91 powder used here and the compositions of Gr91 and Gr92 dictated by pertinent specifications. (*ASTM A213 & A335)

AM Processing

AM processing of the Gr91 powder was undertaken using an EOS 280 machine with a mild steel insert built into a steel build plate. No standard build parameters were available for Gr91 steel. Consequently, the heat input for Gr91 was estimated by multiplying the heat input recommended for 17-4 PH stainless steel by the ratio of the enthalpy required to heat and melt the alloys ($[\int Cp\ dT + \Delta H_f]_{Gr91}$ / $[\int Cp\ dT + \Delta H_f]_{17\text{-}4}$). This value (68.1 J/mm^3) was then used as the center point for a 5x5 matrix where beam power and beam traverse rate were both varied in combinations of ±10% to produce 25 small cubes (0.5”x0.5” x0.5”). The physical layout of the 5x5 matrix of the blocks is shown in Figure 4.

Beam power was varied from 221 W to 270 W, while traverse rate was changed from 675 mm/s to 825 mm/s. These variations produced heat inputs ranging from 55.7 J/mm^3 to 83.2 J/mm^3. The parameters for each of the 25 cubes are listed in Table 2. The blocks were built in a layer-by-layer fashion normal to the z direction typical of AM processes. The direction of deposition for the parallel passes that comprised each layer was rotated by 67° for each layer.

Note that heat inputs along the diagonals of the 5x5 matrix, such as the one shown by the red line, were all nominally identical. After processing, the blocks were removed from the build plate using EDM wire. Each block was metallographically prepared, polished and etched, and was inspected at magnifications up to 1000x using an optical microscope to determine whether full density was achieved.

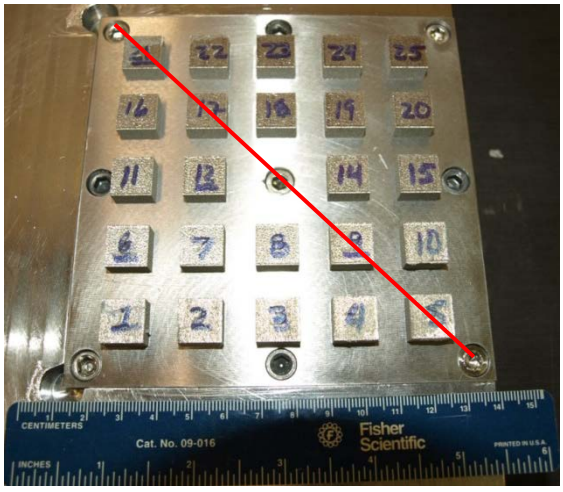

Figure 4 – Block samples on the build plate insert from the 1st build. Heat inputs along the diagonals were all nominally identical.

Later, a second build was carried out to produce a hexagonal shaped prototype, as well as additional samples for tensile testing using an acceptable set of parameters for full density.

Simply put, the overall goal of the project was to tailor the AM process to produce individual AM passes within each layer that transformed to Martensite on cooling, and then arrange so that the adjacent passes in the same layer and passes in the layer(s) above provide partial or complete tempering of the Martensite in-situ to the desired property level. With this approach, the AM component will require no further processing, except for some finish machining. Moreover, the component will have the desired microstructure with proper levels of strength, creep resistance and radiation resistance, while being manufactured more affordably than with current practices.

Heat Treatment

Fully dense blocks were then sectioned further and were given one of three heat-treatments in a vacuum furnace, as listed below:

1) As-deposited (AD) – No heat treatment
2) Direct Tempered (DT) - 770°C for 45 minutes
3) Normalized, Quenched & Tempered - 1070°C for 15 minutes followed by rapid cooling then temper at 770°C for 45 minutes (N&T).

The cooling rate during helium quenching in the vacuum furnace after normalizing was determined at ~5°C/s through the solid-state transformation range. Note that this cooling rate is rapid enough for Martensite formation in accord with the CCT diagram.

Grade 91 Settings					
Layer Thickness	Speed		Power		Hatch distance
40um Nominal	750		245		0.12
Cube #	Speed		Power		Volume Energy Density
	%Nominal	mm/s	%Nominal	Watts	Joules/mm^3
1	10	825	-10	221	55.7
2	5	788	-10	221	58.3
3	0	750	-10	221	61.3
4	-5	713	-10	221	64.5
5	-10	675	-10	221	68.1
6	10	825	-5	233	58.8
7	5	788	-5	233	61.6
8	0	750	-5	233	64.7
9	-5	713	-5	233	68.1
10	-10	675	-5	233	71.8
11	10	825	0	245	61.9
12	5	788	0	245	64.8
13	0	750	0	245	68.1
14	-5	713	0	245	71.6
15	-10	675	0	245	75.6
16	10	825	5	257	65.0
17	5	788	5	257	68.1
18	0	750	5	257	71.5
19	-5	713	5	257	75.2
20	-10	675	5	257	79.4
21	10	825	10	270	68.1
22	5	788	10	270	71.3
23	0	750	10	270	74.9
24	-5	713	10	270	78.8
25	-10	675	10	270	83.2

Table 2– Matrix of build parameters for Gr91.

Characterization

Microstructures of the samples were characterized across several length scales using light optical microscopy (LOM), SEM, EBSD, TEM/STEM and high energy XRD at the Brookhaven Laboratory beamline. Several etchants were used to reveal microstructures for the samples examined with LOM and SEM. The Oxalic acid electro-etch (6V DC for ~20 seconds) was the most commonly used etchant. EBSD samples were typically vibratory polished and electro-polished.

Mechanical Testing

Mounted samples were tested using the Vickers microhardness technique with a load of 200 gms. Various microstructural regions of the samples were also examined using a nano-indentation technique at room temperature. The goal of the second build discussed earlier was to produce the hexagonal prototype component and about 50 tensile samples for subsequent testing in the various heat treatment conditions. Unfortunately, the build stopped prematurely because the recoater arm jammed on one of the tensile samples, leaving all of the samples without a grip section on one end.

Consequently, limited tensile testing was carried out on samples produced from smaller blocks produced during the same build that were intended originally for characterization.

Irradiation Testing

Foils from various microstructural regions for the different heat treatments were removed by FIB and irradiated at the LANL Ion Beam Materials Laboratory (IBML) using 5 MeV Fe^{2} ions at room temperature and at 300°C. The samples were irradiated for times sufficient to produce 3 dpa or 30 dpa of damage. Damage profiles were calculated using SRIM, and are shown in Figure 5.

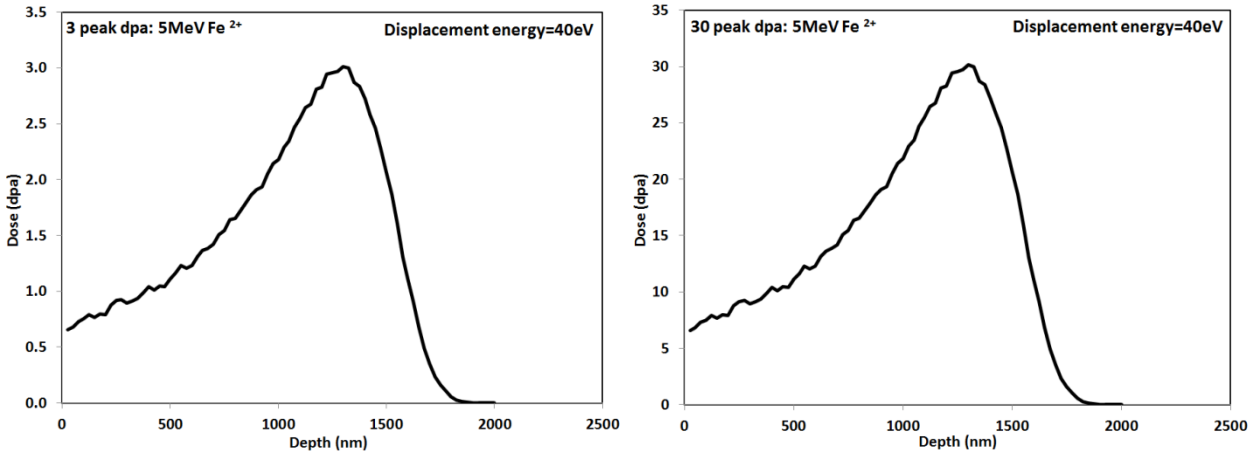

Figure 5 – Damage profiles used for irradiation testing with 5 MeV Fe^{2} ions. Calculated using the SRIM code.

Results – Phase 1(a)

As-Deposited Samples

Low magnification light optical micrographs of an as-deposited (AD) sample are shown in Figures 6 (a) and (b). Individual AM passes can be observed. Note the horizontal pattern of contrast corresponding to individual layers.

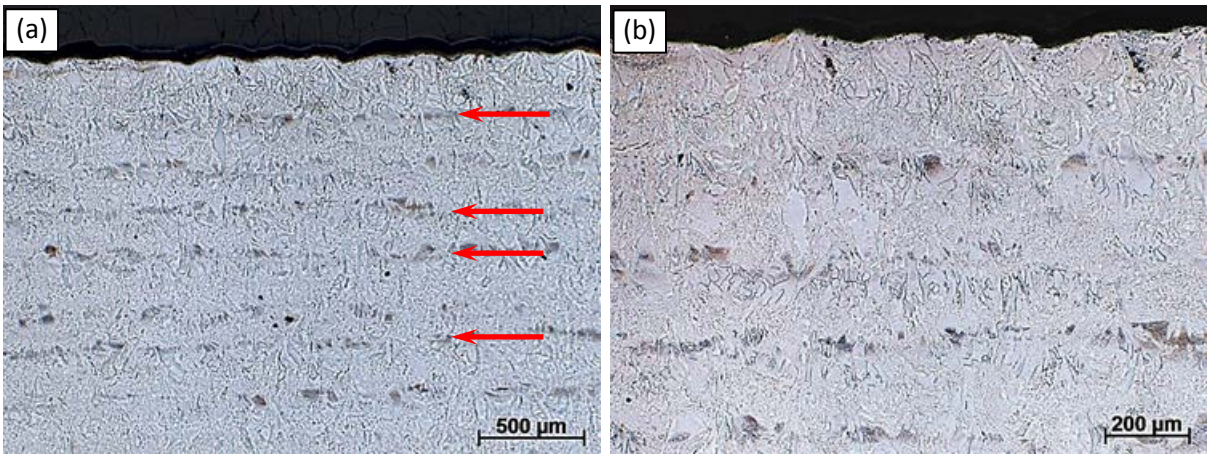

Figure 6 – Light optical micrographs of an as-deposited sample. Note the horizontal pattern of contrast corresponding to individual layers (arrows).

Details of the AD microstructure can be seen in Figure 7. Several distinct features can be identified and are indicated by different numbers for discussion. A cellular structure, characteristic of solidification, is evident in the background. Fusion boundaries between individual AM passes are shown by red arrows (labeled 1). Grain boundaries decorated with carbides after solidification that were removed ("ditched")

by etching with the Oxalic acid etch are indicated by the blue arrows (labeled 2). A featureless, blocky phase can be seen along solidification grain boundaries. This phase is designated by the green arrows (labeled 3) and may have formed via a massive reaction. Finally, clusters of darker colored "speckles" consist of very fine grains with ditched grain boundaries where carbides were removed by etching.

The ditched grain boundaries (blue arrows) and speckles can be seen more clearly in Figure 8(a). It is evident that the carbides along grain boundaries and around the small grains that appear as speckles have been removed by etching. The red arrows show regions characteristic of cellular solidification.

The red arrows again indicate regions characteristic of cellular solidification in Figure 8(b). The featureless, blocky phase also appears along solidification grain boundaries in the same figure. This arrangement suggests that the blocky phase develops when the local region was re-heated by a subsequent AM pass.

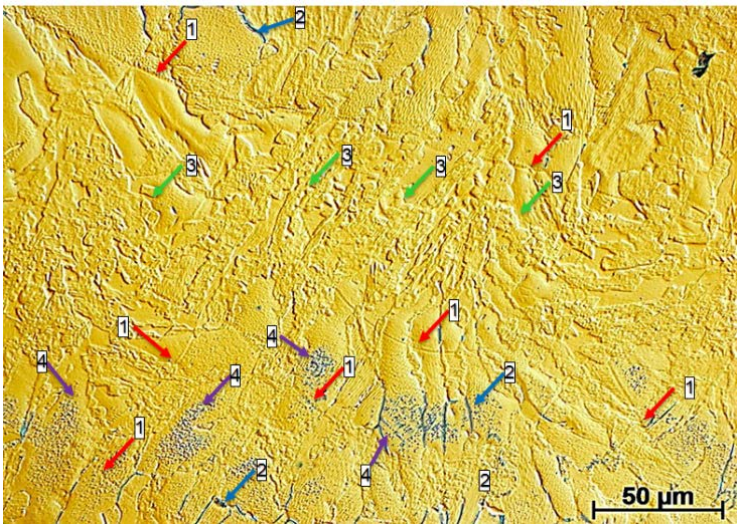

Figure 7 – Light optical micrographs of an as-deposited sample. Features indicated by the different numbers are described in the text.

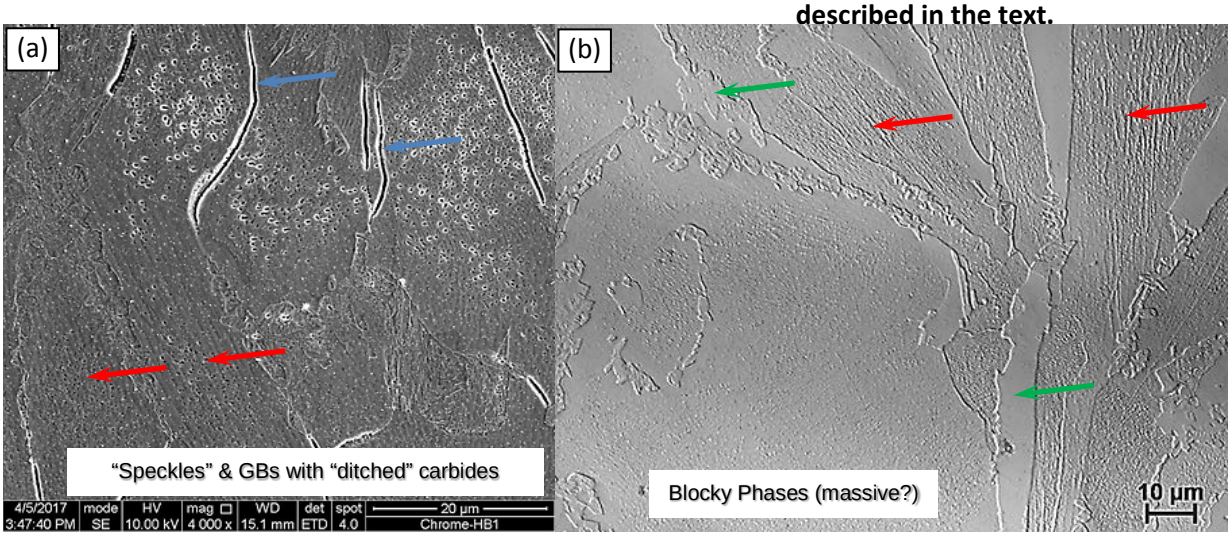

Figure 8 – Micrographs of an as-deposited sample (a) SEM micrograph showing ditched grain boundaries and "speckled" regions; (b) LOM showing blocky phase.

The speckled features can be observed more distinctly at higher magnification in the SEM micrographs in Figures 9(a) and (b). These micrographs were taken using the secondary electron (SE) mode. The green arrows point out regions with cellular solidification structure oriented at ~45°. The red arrows indicate features within fine grains with different morphology to the solidification structure that appear to be laths of Martensite.

The same features are also shown in SEM micrographs taken in the z contract mode (BSE) in Figures 10 (a) and (b). The fan-shaped features are solidification grains for individual AM passes. The arrows in Figure 10 (a) show fine grained regions arranged between the individual AM passes. This arrangement

also suggests that the fine grains formed during re-heating during a later AM pass. The arrows in Figure 10(b), taken at much higher magnification, delineate Martensite laths within the fine grains. Apparently, the Martensite forms when the local regions are reheated in the heat-affected zone (HAZ) of a later pass.

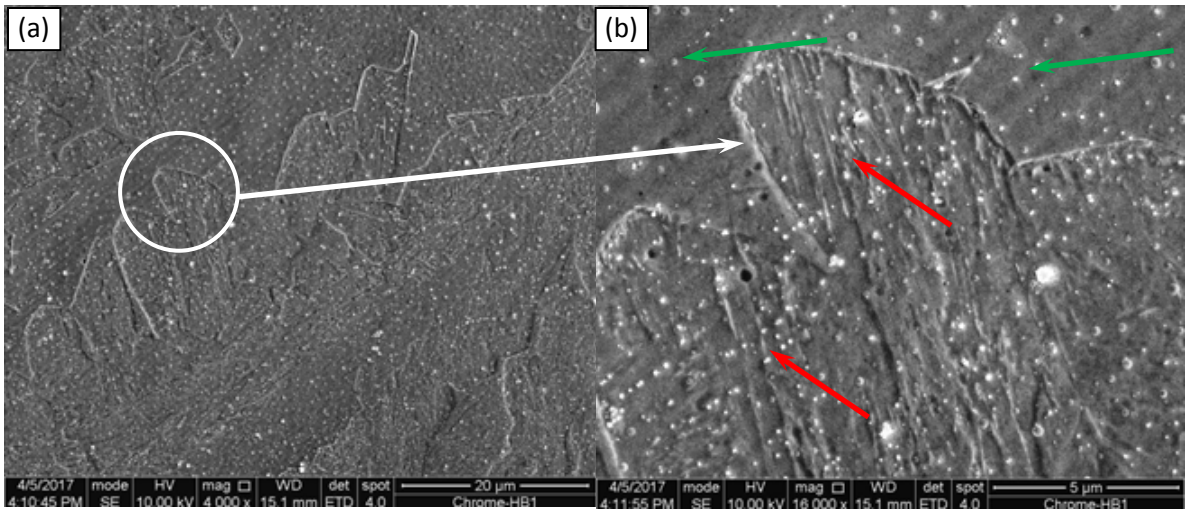

Figure 9 – SEM micrographs of an as-deposited sample corresponding to the "speckled" region shown in Figure 7. Features indicated by the different colored arrows are described in the text.

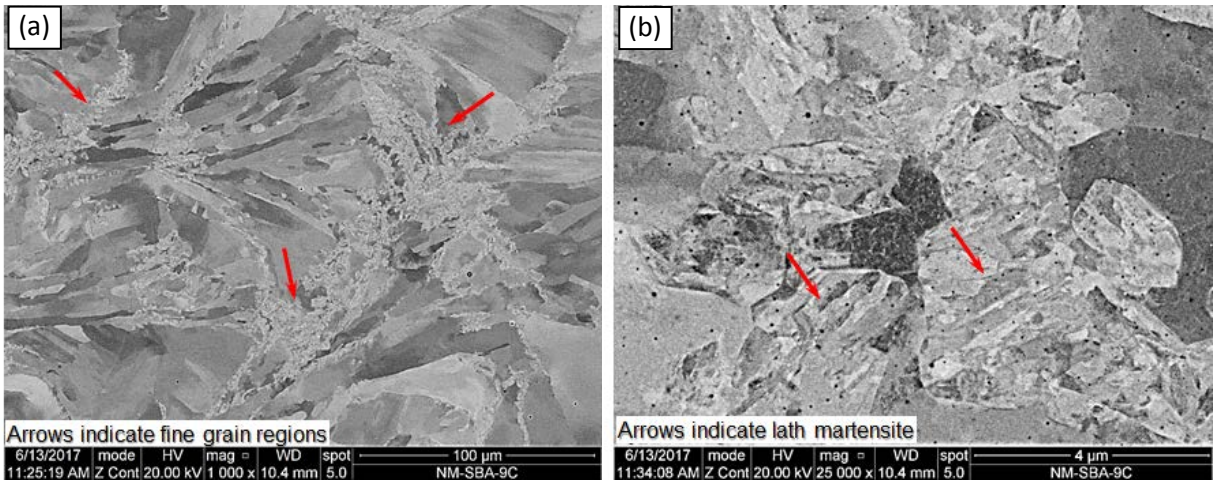

Figure 10 – SEM micrographs of an as-deposited sample corresponding to the "speckled" region.

Interpretation of the origins of the speckle features and the blocky phase is complicated by the large number of individual AM passes present in the transverse metallographic sections and the varying angle of the deposition directions. Observations made to this point suggest that both constituents develop when the region is part of the HAZ of a later pass(es). To aid in interpretation of these features, a pulsed laser weld with simpler geometry was produced on a polished and etched sample from the second AM build of Gr91, Figure 11. The laser pulse length was short (5 ms), and the solidification rate was similar to that in the AM deposits. Note the overlap region of the spot welds like the region shown in the dotted circle. Examination of the overlap region provides some interesting insight into microstructural evolution in the AM deposits. LOMs of the region indicate by the red circle in Figure 11 are presented in Figures 12(a) and (b). In both figures, the fusion zone (FZ) of a laser spot weld can be seen. The fusion boundary between the FZ and the HAZ lying in the FZ of the prior spot weld is indicated by the tips of

the arrows in Figure 12(a). Close inspection of the two micrographs reveals that two distinct HAZs can be identified.

The high temperature HAZ (closest to the FZ) shows evidence of the blocky phase along grain boundaries of the prior spot weld. Note that the blocky phase here is much finer than that found in many locations of the AM deposits. A low temperature HAZ can also be seen at greater distance from the FZ. It is characterized by ditched grain boundaries (arrows in Figure 8(b)) and what appear to be the speckled regions discussed earlier (dashed circle). Further details on the evolution of microstructures in the AM deposits will be provided in the Discussion section.

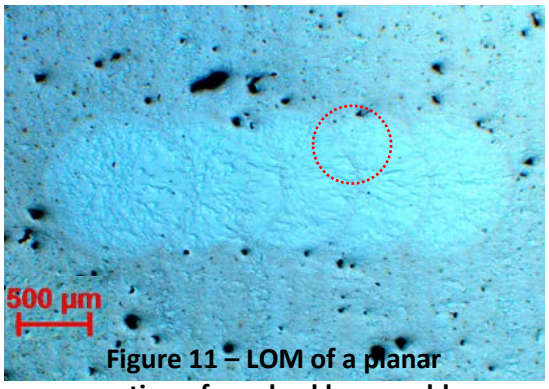

Figure 11 – LOM of a planar section of a pulsed laser weld.

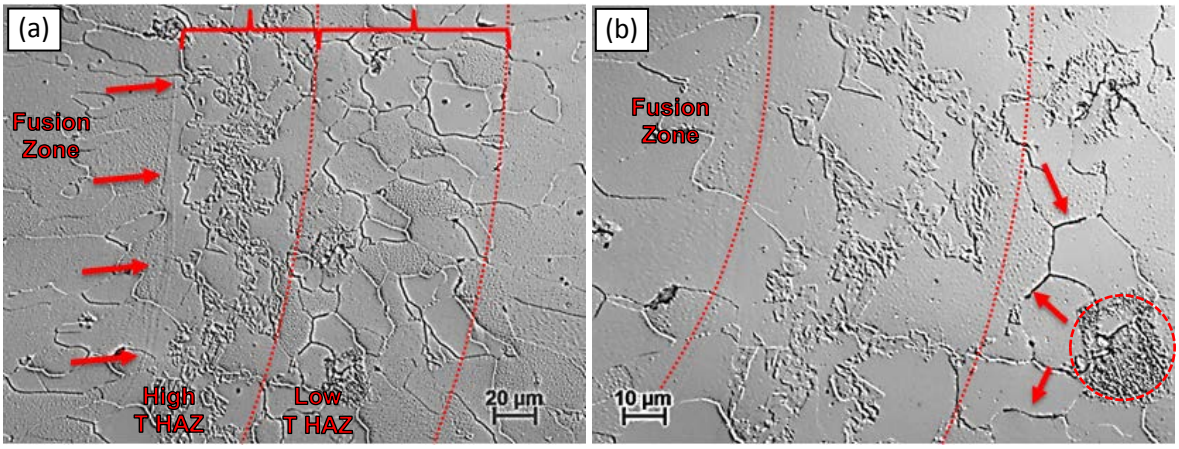

Figure 12 – (a) and (b) LOM of a planar section of a pulsed laser weld showing the existence of two distinct HAZ regions.

Electron Backscattered Diffraction (EBSD) is an SEM based technique that allows determination of certain structural (crystallographic) information. EBSD results from an AD sample are presented in Figures 13(a) to (d). In all of these figures, the build direction is downward. The inverse pole figure (IPF) seen in Figure 13(a) shows the distribution of crystallographic directions (see inset in 13(b)) relative to sample directions. Inspection of the figure corroborates other observations that the speckle features are networks of fine grains along prior solidification grain boundaries and not individual large carbides. The IPF also indicates that the texture is relatively random, likely owing to the 67° pattern for sequential deposition layers.

Image quality (IQ) maps are constructed from electron backscatter diffraction data and provide useful visualizations of microstructure. The contrast in these maps arises from a variety of sources, including phase, strain, topography, and grain boundaries. The dark contrast in Figure 13(b) indicates regions of poor image quality in the fine grained regions of the speckles. Figure 13(c) is an image where the IQ map is overlaid with red lines corresponding to special, low angle grain boundaries (LAGBs), referred to as $\Sigma 3$ boundaries. These observations may be interpreted to suggest that many of the boundaries in the fine-grained regions are LAGBs that result from some type of phase transformation.

Kernel Average Misorientation (KAM) maps are used to determine areas with large misorientation with respect to its neighbors. A false color range is established that corresponds to the value of mis-orientation between crystallographic directions on a pixel-to-pixel basis. The comparison can be chosen as nearest neighbor pixels, or third (or any) nearest neighbor pixels by the user. A cut-off or threshold of

angle of misorientation, often 1°, is selected. Internal strains often show sharp changes from point to point, and if they go significantly beyond the elastic limit, they will typically include dislocations within the sample volume. This situation will be manifest by crystal rotations and a higher value of the KAM (different color). In the KAM map of Figure 13(d), the regions of green color suggest the presence of Martensite. Taken together with the information from the Figures 9, 10 and 13(a)-(c), the speckles appear to be fine grains of Martensite phase with low angle boundaries that formed during reheating in the HAZ of later passes.

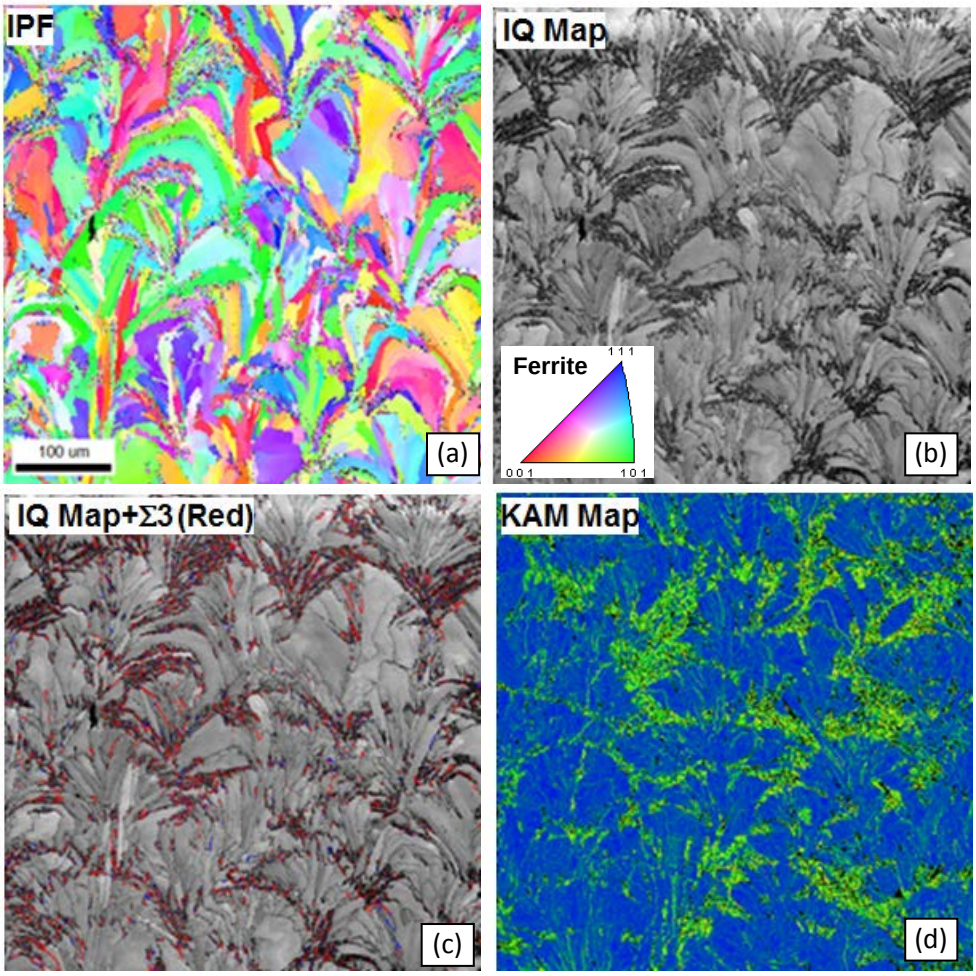

Figure 13 – (a) - (d) Various EBSD maps for the as-deposited sample.

Transmission electron microscopy (TEM) allows for determination of structural (crystallographic) information via diffraction as well as imaging at very high magnifications. TEM foils were extracted from each type of region using focused ion beam (FIB) methods to permit detailed characterization and to tie the nano-scale microstructures to macro-scale features, and ultimately to properties/performance.

A FIB image from an AD sample is shown in Figure 14. TEM foils were removed from three types of areas as

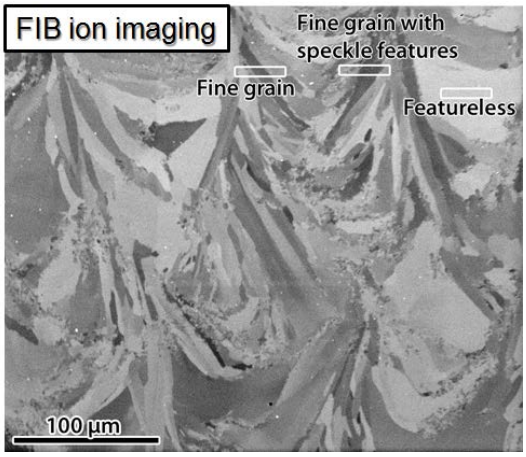

Figure 14 – FIB image showing locations for TEM foil removals.

shown in the figure: 1) fine grain; 2) fine grain with “speckles”; and 3) featureless (blocky) region.
TEM brightfield (BF) micrographs of the different regions of an AD sample are presented in Figures 15(a) to (d). Figure 15(a) shows a BF image of a single grain of the featureless (blocky) region. The microstructure is characterized by platelet features (arrows) that are compositionally invariant with the matrix and are oriented with habit planes near $\langle \mathbf{952} \rangle$ directions of the ferrite (bcc) matrix. They appear to be distributed uniformly with the matrix, and the matrix displays a high dislocation density. If stable, this microstructure has sink sites for point defects in the dislocations and the incoherent platelet interfaces, although the microstructure has fewer sinks than a wrought sample.
Figure 15(b) presents a BF image of the fine grain region of an AD sample. The fine grain regions contain the same microstructural features as the featureless region (i.e. high dislocation density and platelets). However, the grain size is approximately several to ten µm. Again, the dislocations and incoherent platelet interfaces would be sinks for point defects created during irradiation, and the density of sinks is less than in a wrought material.
Examination of another portion of the foil from the same fine grain region reveals additional features, as shown in Figure 15(c). Compositionally invariant regions with high strain are present several µm below the foil surface. These features are the same as those that will be shown below in the speckled region (features are likely Martensite). High strain regions and regions of high dislocation density are present. These regions, if stable during irradiation, would serve as sinks for point defects. However, the wrought material contains more sinks for point defects relatively speaking.

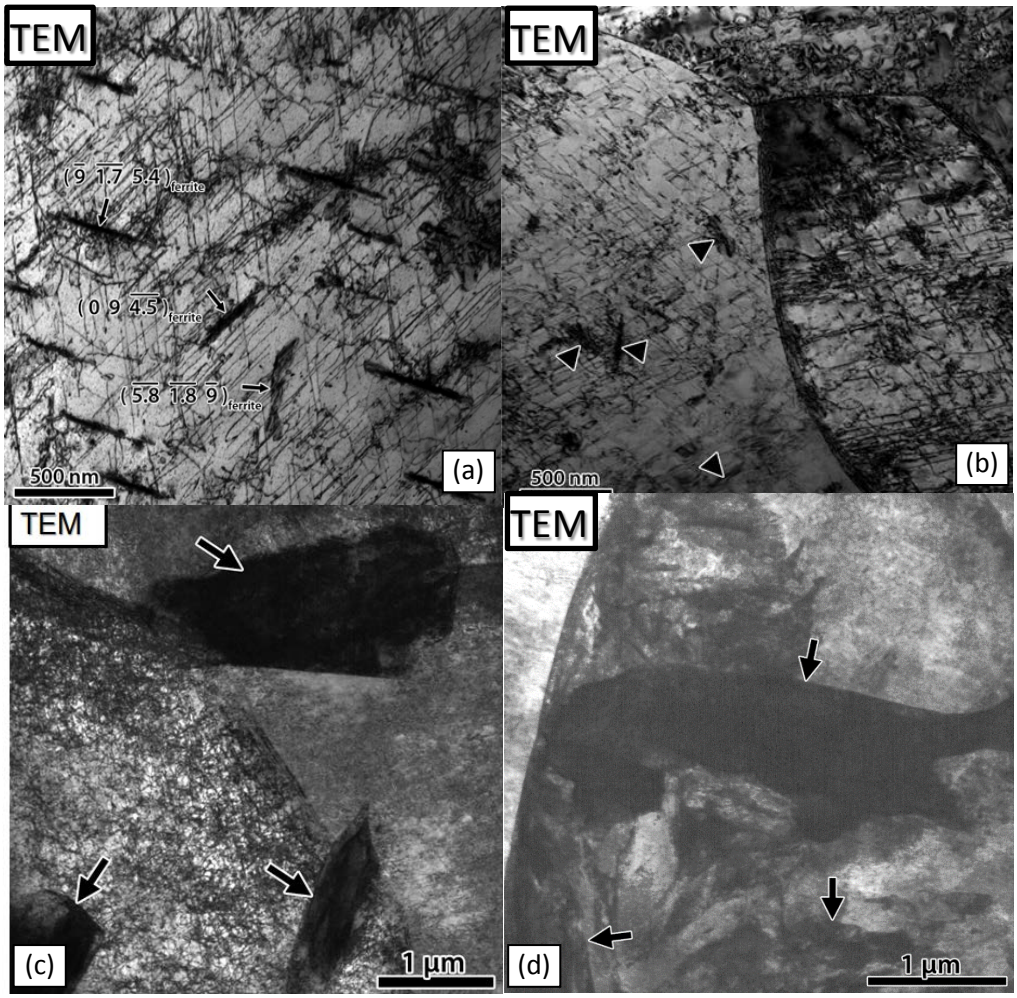

Figure 15 – (a) - (d) TEM BF images for the as-deposited sample.

Finally, a BF image for the speckle region is provided in Figure 15(d). The microstructure is characterized by fine grains that contain large amounts of strain in the form of dislocations, subgrains and what appear to be Martensitic platelets. The fine microstructural features with the high density of dislocations are equivalent to the wrought microstructure in terms of potential for resisting degradation from irradiation damage.

To summarize the results for the AD samples, no Martensite phase was found in the samples with the exception of regions within the fine-grain areas. This result was indeed surprising, and is discussed more in the Discussion section.

Direct Tempered Samples

Results for the direct tempered samples are ommitted here for the sake of brevity. Since no Martensite was found in the AD samples, there was none to temper. Microstructures of the direct tempered samples looked much like those of the AD samples except that there were many more carbides. Grain structures developed during solidification persist.

Normalized, Quenched and Tempered Samples.

Optical micrographs of an N&T sample are shown in Figure 16. The microstructure was more uniform than for the AD samples and is characterized by fine-grained (5 to 20 µm) Martensite. A comparison of the microstructures of an N&T sample produced using AM and a wrought sample also in the N&T condition is given in Figures 17(a) and (b). Both samples have a Martensitic microstructure. However, note the finer prior austenite grain size and much finer lath spacing of the AM N&T sample relative to the wrought sample. These features may be expected to result in higher strength and irradiation tolerance of the AM N&T sample. The microstructural refinement attendant with the AM N&T sample likely originated from the finer solidification grain size and higher dislocation density of the AM N&T sample relative to the wrought sample.

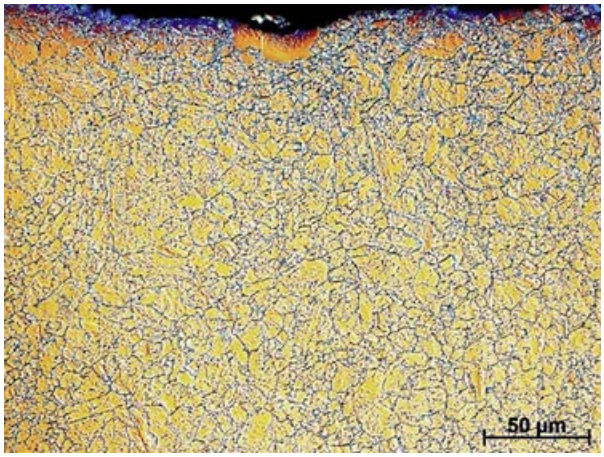

Figure 16 – LOM of an N&T sample.

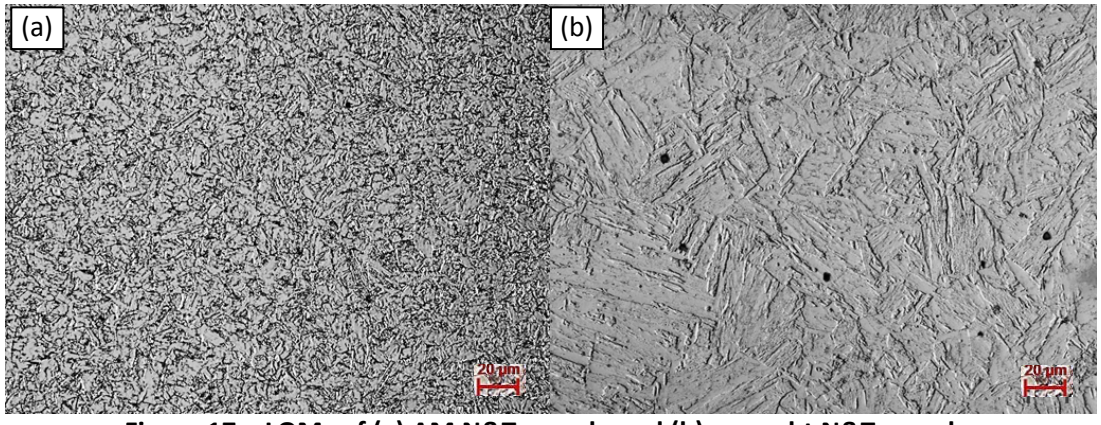

Figure 17 – LOMs of (a) AM N&T sample and (b) wrought N&T sample.

SEM micrographs of an AM N&T sample are presented in Figures 18(a) and (b). Holes along grain boundaries and in grain interiors resulted from removal of carbides from these locations due to the Oxalic acid etch. These and other carbides formed during the tempering part of the heat-treatment.

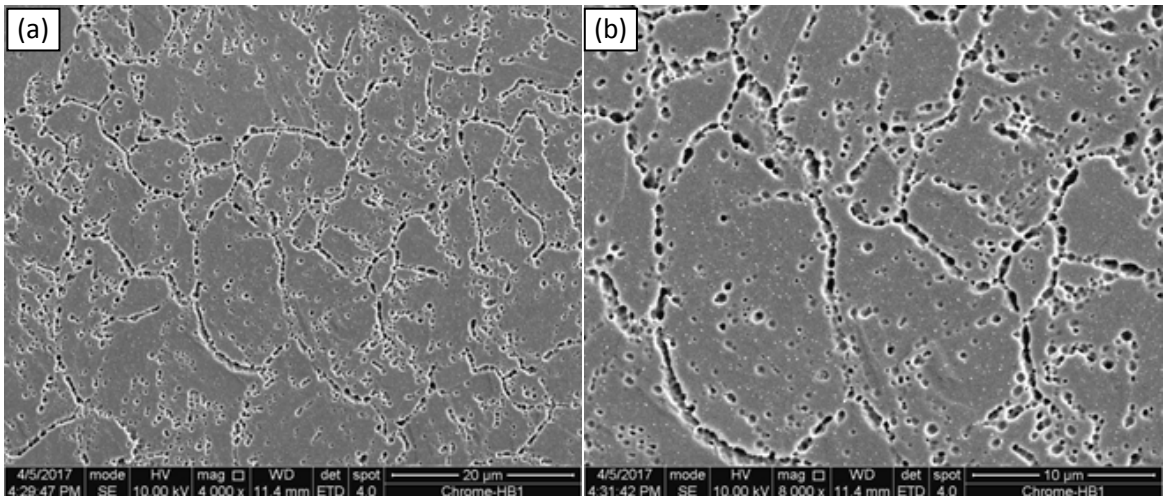

Figure 18 – SEM micrographs of the AM N&T sample.

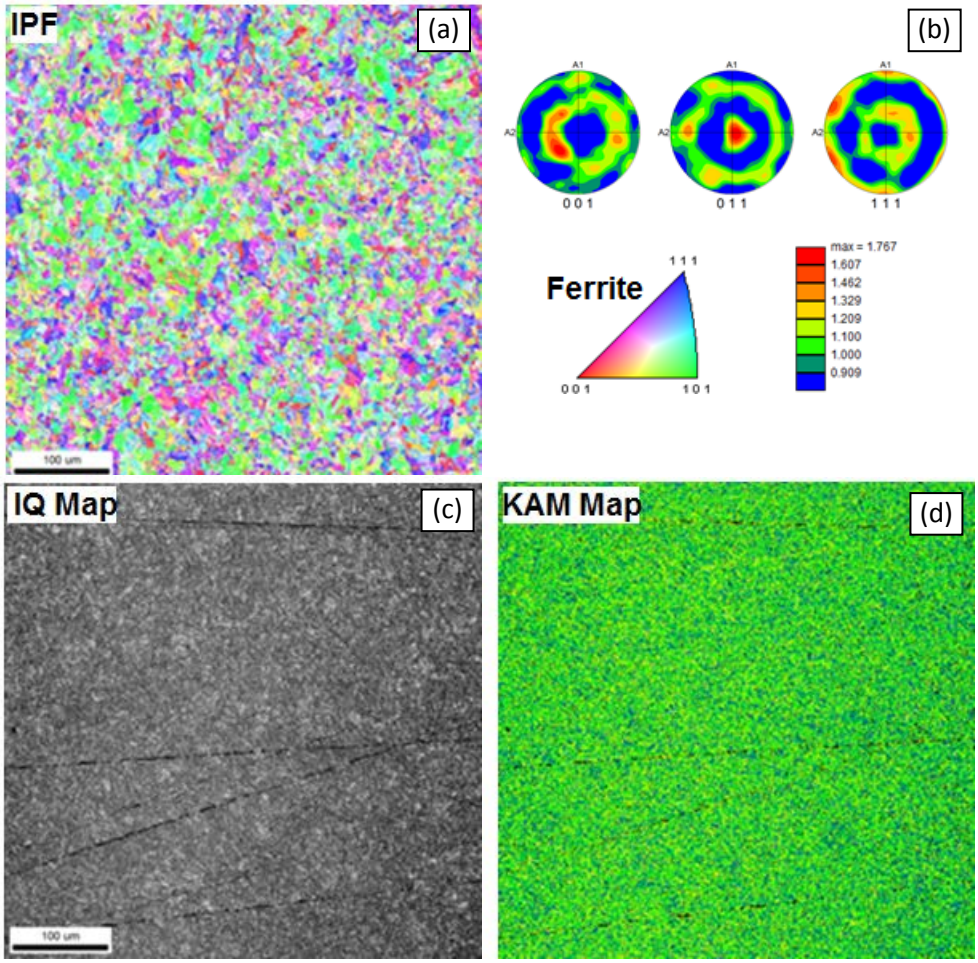

Figure 19 – Various EBSD maps for the N&T sample.

Results from EBSD investigations with an N&T sample are shown in Figure 19(a) – (d). The IPF image indicates that the sample exhibits a random texture, although the pole figures suggest some degree of texture features. The IPF also confirms the fine grain size of the sample after heat-treatment. The uniform contrast of the IQ map (except for a few scratches) is consistent with a uniform microstructure. Finally, the uniform green color of the KAM map suggests that the entire microstructure is most likely Martensitic.

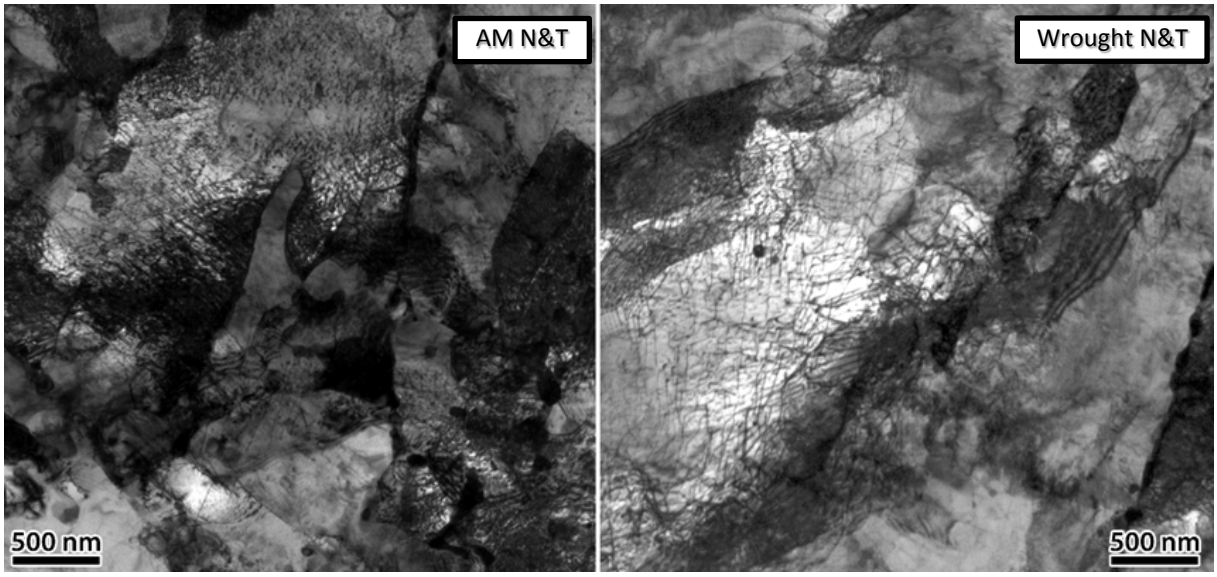

Figure 20 – (a) and (b) TEM BF images for an N&T sample.

TEM BF images of an N&T sample are presented in Figures 20(a) and (b). The microstructure of this sample is similar to the wrought samples except the grain size is much finer here. The dislocation density here is very high, and carbides are found along the grain boundaries. An interesting feature not seen previously at lower magnifications is the presence of very small gas pores (not shown), likely developed during solidification due the drop in solubility of gas species. The volume fraction of pores was estimated to be on the order of 0.1% with an average diameter of ~25 nm. It is interesting to note that these pores may be useful as sites for He gas formed during irradiation.

Summary

A summary of microstructural features for the three types of sample (AD, DT and N&T) is provided in Table 3.

	AD	DT	N&T
Carbides	**None or few**	**Carbides on gbs and grain interiors**	**Carbides on gbs and grain interiors**
Features	**High strain regions with Martensite**	**High strain regions transform to small grains & carbides**	**High dislocation density and small grains**
Homogeneity	**Inhomogeneous**	**Inhomogeneous**	**Homogeneous**
Pores		**yes**	**yes**

Table 3– Summary of selected microstructural features in different samples.

Tensile Properties

Recall that the number of tensile samples was limited due to a crash of the AM system. As a result, only two samples of each sample type were tested. A summary of the results of tensile testing is provided in Table 4. A key to the abbreviations used in this table and Figure 21 is also shown below.

Sample ID	Yield Strength (MPa)	Ultimate Strength (MPa)
WQ 1	1006	1304
WQ 2	1009	1270
WQT 1	610	791
WQT 2	612	792
AD 1	805	1009
AD2	808	1023
Q 1	980	1325
Q 2	942	1212
T 1	482	706
T 2	482	701
QT 1	532	740
QT 2	532	740

Table 3– Summary of tensile test results.

Tensile curves for the "best" result for AM and wrought samples in each heat treat condition are shown in Figure 21. Curves are identified by color in the legend. The AM quenched sample had slightly higher TS than the wrought quenched sample, but somewhat lower elongation to failure. The AM Q&T sample showed lower YS, TS and elongation to failure relative to the wrought Q&T sample. The AM AD sample showed behavior intermediate to the quenched and Q&T samples.

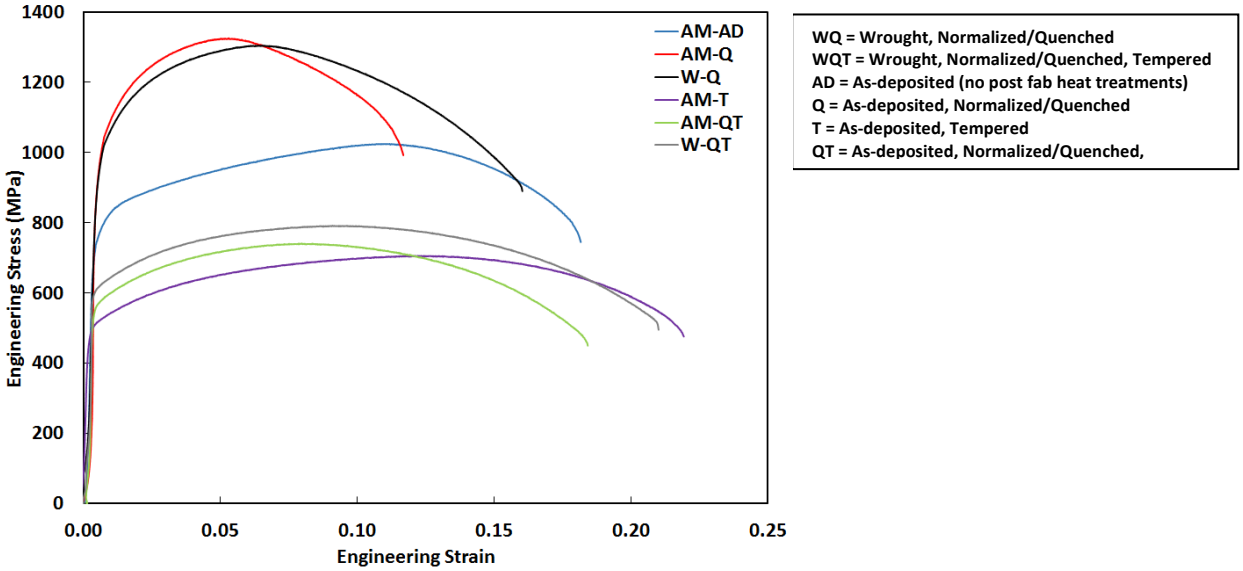

Figure 21 – Best tensile curve for each type of sample.

A comparison of YS and hardness for the AM samples and wrought samples of Gr91 is found in Figure 22. Given the limited data, it appears that the AM samples perform similarly to the wrought samples.

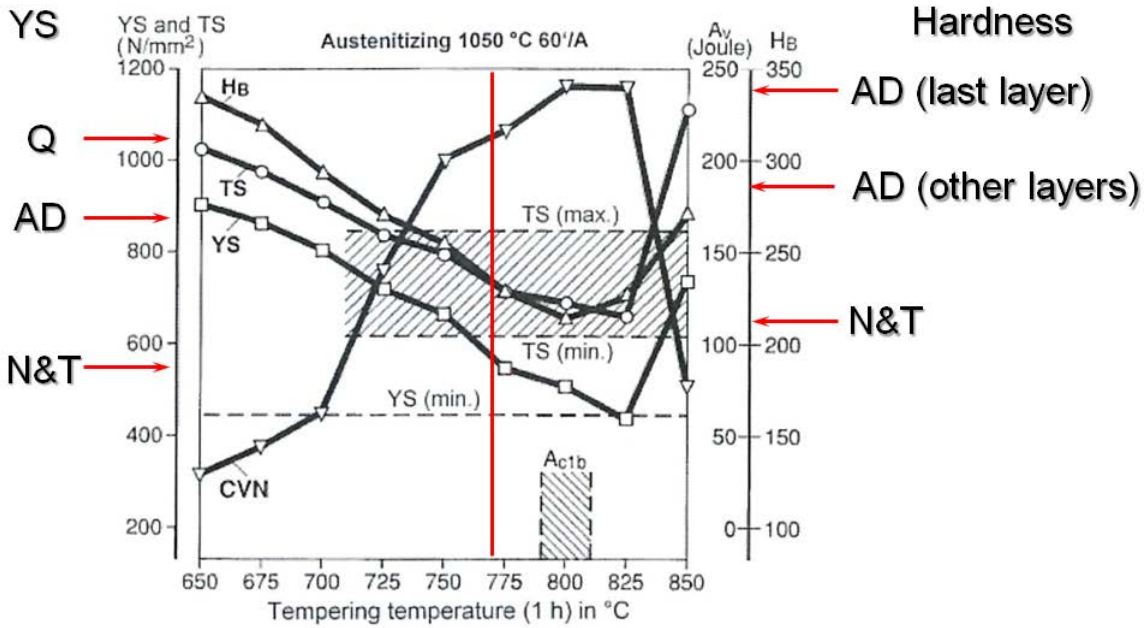

Figure 22 – Comparison of YS and hardness with wrought samples.

Prototype

A photograph of the prototype hexagon produced in Phase 1 is shown in Figure 22. The partly built tensile samples can be seen in the center of the hexagon. The four blocks seen at the back right corner were used to produce the limited number of tensile sample.

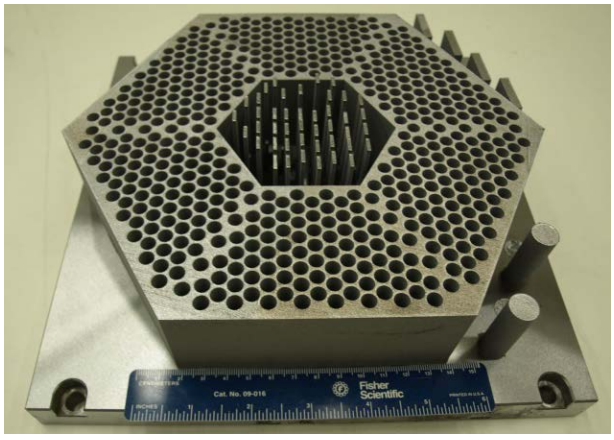

Figure 21 – Subscale prototype hexagonal component.

Results – Phase 1(b)

Discussion of results from Phase 1(b) is limited for the sake of brevity. The most important result from this period involved performing AM using a different type of AM process. The directed-energy AM process is different from the powder bed method used in Phase 1(a).

A new batch of powder, with a larger size distribution was purchased and used to make AM deposits using the LENS DE type machine. The key difference here was that the deposition rate was much lower (~30 ipm vs ~1800 ipm) than that used with the EOS machine. The result was as expected for the Gr91 (and as previously expected for the EOS), i.e. the resultant microstructure was Martensitic, Figure 22. Moreover, the goal stated earlier involving in-situ tempering was realized as the hardness of the deposit was nearly identical to that desired of Gr91 components in service without the need for post AM heat treatment.

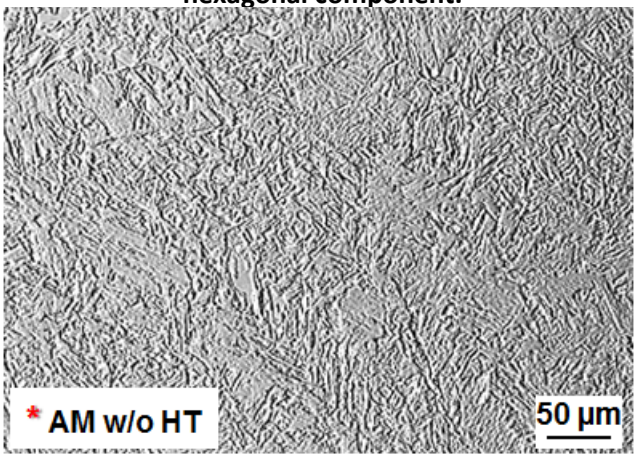

Figure 22 – Microstructure of Gr91 deposit produced using the LENS DE AM process.

Discussion

As mentioned earlier, no Martensite phase was found in the AD samples with the exception of regions within the fine-grain areas. This result was indeed surprising with respect to the CCT diagram shown in Figure 2. Cooling rates through the solidification range were estimated at ~10^5 K/s using published relationships and dendrite arm spacing measurements. Given these rapid cooling rates for solidification, it is reasonable to expect cooling rates for the solid-state transformation of austenite (FCC phase, see phase diagram in Figure 1) to be rapid enough to form Martensite rather that ferrite (bcc phase found in all characterization studies discussed earlier, with the exception of the speckle regions). In other words, if the austenite phase existed, the cooling rates experienced should have resulted in Martensite.

These observations were unexpected and defied traditional phase transformation theories. The only rational explanation for this behavior is that the rapid processing led to some non-equilibrium condition. The existence of solidification structures in the room temperature microstructure is further evidence for non-equilibrium behavior. Evidence of solidification structures in steels of this type are always "erased" by the solid-state transformations within the room temperature microstructures, even for rapid laser welding. This result is extremely interesting from a scientific viewpoint and merits further study.

Microstructures of the DT samples were consistent with coarsening of carbides by diffusion during the heat-treatment. Grain structures developed during solidification persisted after heat-treatment.

Microstructures of the N&T samples were consistent with re-austenization followed by quenching and tempering. All evidence of the structures developed during solidification was erased, and were replaced with equiaxed grains with carbides, as anticipated. This result itself represents some success toward the goals of this project.

Finally, achievement of Martensite using the LENS DE process during Phase 1(b) demonstrated convincingly that AM can be used successfully for Gr91 steel. Moreover, this event also confirmed that original hypothesis that AM can be used for successful in-situ tempering by exploiting the thermal cycles of subsequent AM passes.

Conclusions

1) Surprisingly, no Martensite phase was found in the AD samples with the exception of regions within the fine-grain areas. This result was indeed unusual with respect to the CCT diagram.
2) This observation with the AD samples was unexpected and defied traditional phase transformation theories. The only rational explanation for this behavior is that the rapid processing led to some non-equilibrium condition.
3) The existence of solidification structures in the room temperature microstructure is further evidence for non-equilibrium behavior in the AD samples.
4) Microstructures of the N&T samples were consistent with re-austenization followed by quenching and tempering. All evidence of the structures developed during solidification was erased, and were replaced with equiaxed grains with carbides, as anticipated. This result itself represents some success toward the goals of this project.
5) Achievement of Martensite using the LENS DE process during Phase 1(b) demonstrated convincingly that AM can be used successfully for Gr91 steel. Moreover, this event also confirmed the original hypothesis that AM can be used for successful in-situ tempering by exploiting the thermal cycles of subsequent AM passes.